

The Natural Helmholtz-Hodge Decomposition for Open-Boundary Flow Analysis

Harsh Bhatia, *Student Member, IEEE*, Valerio Pascucci, *Member, IEEE*, and Peer-Timo Bremer, *Member, IEEE*

Abstract—The Helmholtz-Hodge decomposition (HHD), which describes a flow as the sum of an incompressible, an irrotational, and a harmonic flow, is a fundamental tool for simulation and analysis. Unfortunately, for bounded domains, the HHD is not uniquely defined, traditionally, boundary conditions are imposed to obtain a unique solution. However, in general, the boundary conditions used during the simulation may not be known, or the simulation may use open boundary conditions. In these cases, the flow imposed by traditional boundary conditions may not be compatible with the given data, which leads to sometimes drastic artifacts and distortions in all three components, hence producing unphysical results. This paper proposes the *natural HHD*, which is defined by separating the flow into internal and external components. Using a completely data-driven approach, the proposed technique obtains uniqueness without assuming boundary conditions a priori. As a result, it enables a reliable and artifact-free analysis for flows with open boundaries or unknown boundary conditions. Furthermore, our approach computes the HHD on a point-wise basis in contrast to the existing global techniques, and thus supports computing inexpensive local approximations for any subset of the domain. Finally, the technique is easy to implement for a variety of spatial discretizations and interpolated fields in both two and three dimensions.

Index Terms—The Helmholtz-Hodge decomposition, vector fields, boundary conditions, uniqueness, harmonic flows

1 INTRODUCTION

ANALYSIS of flows plays an integral role in understanding physical phenomena such as eddies in the ocean [1], weather [2], combustion [3], [4], [5], or solar convection in astrophysics [6]. Large-scale scientific simulations and observations create complex flows which encapsulate important information about these underlying phenomena. In order to gain insights from such flows, the *Helmholtz-Hodge decomposition (HHD)* [7] is widely used as a valuable analysis tool.

The HHD describes a flow field as the sum of a *divergence-free* (incompressible), a *rotation-free* (irrotational), and a *harmonic* (translational) component. Such a description may simplify the analysis of complex flows by studying the divergence- and rotation-related properties separately. For example, flow features such as critical points [8], and indicator functions such as vorticity [9], [10] or compressibility are studied as parts of simpler component flows (e.g., in [11], [12], [13]). Furthermore, the incompressible and irrotational components can also be defined in terms of potential functions, which are typically easier to analyze, and provide meaningful information, e.g., in the study of Alzheimers disease [14]. In the

2D case, these potentials are scalar, and are used in a variety of applications such as streamline seeding [15] or finger print matching [16].

On unbounded domains, the HHD is unique for flows vanishing at infinity. However, most practical cases deal with flows on bounded domains, where the HHD is not unique. In order to obtain a unique decomposition in such cases, traditional techniques enforce *boundary conditions*, which prescribe the component flows along the boundary, e.g., that the irrotational flow must be normal, and the incompressible flow parallel to the boundary.

However, many flows are generated through simulations, and the boundary conditions used during the simulation may not be known during the analysis or too complex to be incorporated. Furthermore, a large number of simulations instead use an *open boundary*, where the flow at all or part of the boundary is observed as the output of the simulation, e.g., in large-scale combustion simulations [3], [4], [5], [17], [18], free surface fluid animations [19], or oceanography [20]. In such cases, default boundary conditions may be incompatible with the data, and lead to unphysical results.

Instead, we propose a new strategy to obtain uniqueness in the HHD. Using concepts from potential theory, we consider a given flow to be the sum of flows created due to *internal* and *external* influences with respect to a given bounded domain. In this context, the traditional way of imposing boundary conditions is equivalent to presuming to know the external influences, thus leading to a unique identification of flow due to internal influences. In contrast, our approach reverses the process by computing the flow due to the internal influences using the given data, uniquely and without any assumptions. The residual is then considered to be the flow due to

• H. Bhatia and P.-T. Bremer are with the Scientific Computing and Imaging Institute, University of Utah, Salt Lake City, UT 84112, and the Lawrence Livermore National Laboratory, Livermore, CA 94550. E-mail: {hbhatia, ptbremer}@sci.utah.edu.

• V. Pascucci is with the Scientific Computing and Imaging Institute, University of Utah, Salt Lake City, UT 84112. E-mail: pascucci@sci.utah.edu.

Manuscript received 16 Oct. 2013; revised 11 Feb. 2014; accepted 27 Feb. 2014. Date of publication 16 Mar. 2014; date of current version 1 Nov. 2014.

Recommended for acceptance by D. Weiskopf.

For information on obtaining reprints of this article, please send e-mail to: reprints@ieee.org, and reference the Digital Object Identifier below.

Digital Object Identifier no. 10.1109/TVCG.2014.2312012

external influences. As a result, the proposed HHD is unique without prescribing boundary conditions. Consequently, no artificial features are introduced in the components due to boundary conditions, and the proposed decomposition naturally determines the component flows along the boundary in a data-driven manner. Therefore, we refer to it as the *natural HHD*.

Contributions. To address the challenges of non-uniqueness in the HHD of a given flow $\vec{\xi}$ on a subset Ω of \mathbb{R}^n , for $n = 2, 3$, we

- 1) define the *natural HHD* of $\vec{\xi}$ as its decomposition into *internal* flow explained by the divergence and rotation of $\vec{\xi}$, and *external* flow due to unknown influences from outside;
- 2) show that this decomposition is unique without needing any boundary conditions;
- 3) introduce efficient *local computation* and *local approximation* of the natural HHD, which restrict computation to a subset of Ω ;
- 4) present a simple and embarrassingly parallel algorithm to compute the natural HHD for a variety of spatial discretizations and interpolated vector fields in both 2D and 3D, and compare it to the state-of-the-art using several synthetic and real-world data, demonstrating that it is stable, well-behaved, and produces no artifacts; and
- 5) propose a metric to, for the first time, quantify the amount of harmonic flow present in $\vec{\xi}$.

2 UNDERSTANDING HARMONIC FLOW

The fundamental reason for non-uniqueness in the HHD is that harmonic flows are both irrotational and incompressible. Therefore, one can add an arbitrary harmonic flow to any one of the three HHD components, and its negative to another, to obtain a different valid decomposition. As a result, any two valid HHDs differ in only how the harmonic flow is represented. Therefore, to address non-uniqueness, we must first understand the nature of harmonic flows,

how they are related to boundary conditions, and why imposing boundary conditions may not be a good choice.

Traditionally, uniqueness is obtained by imposing boundary conditions, which add certain harmonic flows to the incompressible and irrotational components to match the imposed boundary flow, and their negative to the harmonic component, which is then computed as the residual. For example, the most common boundary conditions require the irrotational and incompressible components to be normal and parallel to the boundary, respectively.

However, these conditions are somewhat arbitrary, and may not be compatible with the given flow. For example, consider the rotational flow shown in Fig. 1. Through the HHD of this field, one would expect to recover the same flow as the incompressible component, while the other two components being zero. However, as the figure illustrates, the obtained incompressible component contains serious artifacts. Especially notice the change in topology of the output field. These artifacts are caused due to the fact that the HHD imposes a parallel flow on the boundary—a configuration incompatible with the original flow.

In general, the boundary conditions create a strong coupling between the component flows and the shape and orientation of the boundary. As shown in Fig. 6, when the same analytical flow is sampled on differently shaped domains, one obtains markedly different decompositions. Using these decompositions for analysis may produce significantly different results for the same flow depending on the shape of the domain. Given that the shape of the domain is usually determined by the region of interest and/or practical considerations such as mesh type or compute power, this dependency calls such analysis into question.

Intuitively, these examples suggest the need to identify the harmonic flow independent of the shape and orientation of the boundary. However, the harmonic flow is always defined with respect to the viewpoint of the observer. As seen in the Fig. 2, the translational flow in Ω is harmonic, and one would presume its HHD should contain only a harmonic component. However, considering the domain Ω' instead, some of this translational flow is clearly created and destroyed by the local divergence (in red and green), and is therefore not harmonic. As a result, the irrotational component of the HHD on Ω' should be non-zero in Ω .

It is well known that harmonic functions are associated with boundary conditions, which equivalently means that they depend upon the phenomena occurring outside the given domain. However, since external information is

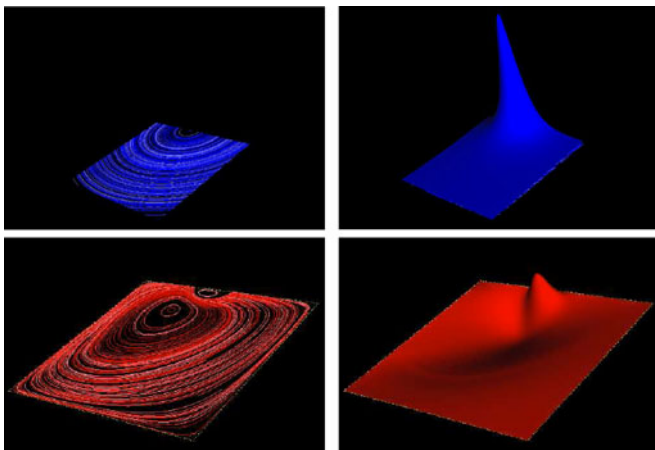


Fig. 1. An example given by Wiebel [21] to show artifacts of the HHD boundary conditions. Top: A rotational vector field (left) and the potential function used to create it (right). Bottom: The incompressible component and its potential function recovered through the HHD. Note that the rotation is inverted and an additional critical point is introduced in the output field.

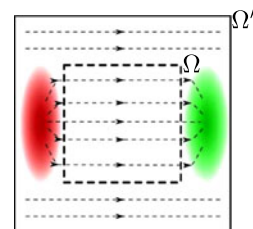


Fig. 2. Definition of harmonic flow depends on the domain considered. The translational flow in Ω is harmonic with respect to Ω , but may not be harmonic with respect to Ω' , depending upon the flow in Ω'/Ω .

usually unknown, identifying harmonic flows by imposing boundary conditions on Ω is equivalent to presuming to know the flow on Ω' or rather its influence on Ω . In contrast, we argue that any non-harmonic flow can be completely explained by the information available inside the domain. Therefore, a harmonic flow can be indirectly identified as the flow that cannot be explained by the available data inside the given domain. Such an interpretation is completely data-driven, and makes no assumptions about unknown external information.

This indirect interpretation of harmonic flow has an important advantage. So far, there exists no technique that can use the divergence and curl of a given flow to determine whether it “contains” a non-zero harmonic flow or not. However, considering the presented interpretation, it becomes possible to implicitly identify any harmonic flow with respect to a given domain. Using this interpretation of harmonic flows, the natural HHD obtains uniqueness without assuming any boundary conditions a priori, and we argue that it is more suited for the purpose of data analysis, since it does not assume potentially inaccurate information.

The practical utility of the natural HHD is that it allows an open-boundary flow analysis, which is essential for a variety of applications, some of which are briefly discussed in Section 3. Furthermore, in a large number of flow simulations, the goal is to study the phenomena intrinsic to the domain, e.g., to understand the turbulence caused by combustion inside the domain (cf. Figs. 8 and 11). In such cases, there is a need for analysis that can successfully separate the influences of internal and external phenomena in a natural way without imposing boundary conditions.

3 RELATED WORK

Open boundaries are an important concept in situations where the flow is expected to move across the simulation domain. For example, in oceanography, when the simulation domain is not bound by a shoreline. In this context, Lekien et al. [20] perform an open-boundary modal analysis and discuss corresponding boundary conditions. The recent work of Söderström et al. [19] propose a perfectly matched layer (PML)-based approach to obtain non-reflective boundary in simulation of waves. They create artificial sources/sinks to absorb the mass and energy of the waves travelling outwards in order to avoid reflections. The quality of the results, however, depend upon the width of the dampening region.

Besides, there exist a large number of flow simulations such as the flow behind the cylinder, lifted jet flame [4], [5], jet in cross-flow [17], [18], where flow is injected in the domain from one side, and the response of the system is studied along with the outflux of the flow from the other side.

The particular issue of boundary conditions has been a topic of interest in the context of the HHD as well. Several boundary conditions have been studied in order to find the most “natural” ones to address the boundary artifacts. In most approaches in fluids simulation, however, the boundary conditions are guided by the underlying fluid model. E and Liu [22] compared the numerical convergence of the Dirichlet and Neumann boundary conditions for the projection method (HHD), and concluded that the Neumann boundary conditions provide better accuracy and

convergence than the Dirichlet ones. Denaro [23] summarizes Neumann boundary conditions in detail, and also mentions periodic boundary.

Various techniques have also been discussed for the computation of the discrete HHD. Polthier and Preuß pioneered the modern approach for its computation on surfaces. They propose a global variational approach to compute the scalar potentials [24], and present an algorithm based on a least squares-finite elements method (LS-FEM) to compute the HHD for piecewise constant (PC) vector fields on triangular meshes [25]. Tong et al. [26] extend their work to 3D by computing the decomposition for PC vector fields on tetrahedral meshes. On the other hand, Guo et al. [27] specialize Polthier’s framework for regular grids, by decomposing the regular grid into a regular triangulation and making appropriate optimizations. Petronetto et al. [28] compute the HHD for 2D point-clouds using a smoothed particle hydrodynamics (SPH) approach. Rather than specializing for a particular domain, our framework trivially applies to bilinear/trilinear, and PC vector fields in 2D and 3D.

The earlier methods to compute the HHD are mainly focused on fluid simulation and/or graphics and animation [29], [30], [31], [32]. However, the choice of time and space discretization is guided by the prime objective—simulation/animation, and HHD computation forms a smaller part of the bigger pipeline. There exist other methods to compute the HHD, e.g., in Fourier [11], [33] and wavelets domain [34], using statistical learning [35], etc. A detailed discussion on the methods for the computation of discrete HHD can be found in a recent survey [36].

A flow decomposition based on a similar idea to ours was proposed by Wiebel et al. [37], which represents a flow as the sum of a *potential* and a *localized* flow. The latter captures the local properties of the flow by representing its divergence and rotation inside the domain, while the former has no divergence and rotation, and matches the original flow at the boundary of the domain. In general, their technique can be seen as an incomplete variant of the HHD, which, however, has certain drawbacks. First of all, the computation of the potential flow imposes boundary conditions, which, as discussed above, assumes unknown information about the external influence. Furthermore, the localized flow is always confined within the domain, i.e., its component normal to the boundary is zero. This is a strong assumption, especially for compressible flows. For example, consider a nodal source in a closed domain, where one must expect the flow created due to the source to go across the boundary, something not possible in a localized flow. The technique also needs additional information (material density) to resolve compressible flows. And finally, as discussed by the authors [37], the material density should be near constant for the technique to apply to unsteady flows. In contrast, our technique decomposes the flow into internal and external components in a natural way, without needing any additional information, and produces components uniquely without boundary conditions.

4 MATHEMATICAL BACKGROUND

The HHD is computed by finding a pair of potential functions whose gradient and curl represent the rotation-free

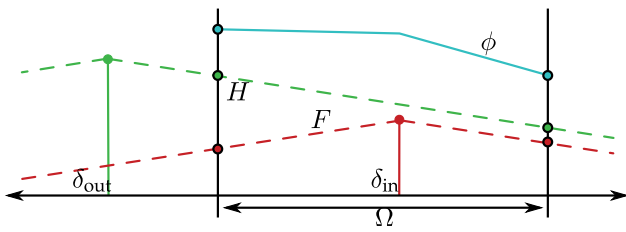


Fig. 3. An illustration of the Poisson equation on $\Omega \subset \mathbb{R}$. Inside Ω , the potential due to an internal source δ_{in} (red) is uniquely defined. However, the potential due to any external source (e.g., δ_{out}) (green) is harmonic (constant slope) inside Ω , and can be determined uniquely using boundary values. Therefore, the solution to the Poisson equation (cyan), i.e., the potential due to interior and exterior sources, is uniquely defined using the boundary conditions.

and divergence-free components. These potentials are computed by solving two Poisson equations. Therefore, it is important to first understand the theory and physical meaning of the Poisson equation and potential functions. In the context of this discussion, the term source represents an energy source giving rise to a potential function, and should not be confused with a critical point of the vector field.

4.1 Potential Theory

One of the most fundamental elliptic partial differential equations is the *Poisson equation*,

$$\nabla^2 \phi = f \quad \text{in } \Omega, \tag{1}$$

where, f is called the *source function*, and ϕ the *potential function*. The general solution to (1) is given by $\phi = F + H$, where $\nabla^2 F = f$, and H is a solution of the *Laplace equation*,

$$\nabla^2 H = 0 \quad \text{in } \Omega, \tag{2}$$

and is called a *harmonic function*. Note that, one can add any harmonic function H to ϕ while still satisfying (1). To obtain a *particular solution* to the Poisson equation (1), one needs to choose a specific H , typically done by imposing boundary conditions.

In physical terms (cf. Fig. 3), the Poisson equation (1) solves for the potential ϕ generated by the (energy) sources *inside* the domain (defined by f), as well as those *outside* the domain. However, since for the Laplace equation (2), the (energy) sources are zero inside the domain, its solution (a harmonic function) represents the *external influence* [38], [39], i.e., the potential generated by the (energy) sources lying outside Ω .

The external influence can be inferred if its boundary values are known. Therefore, the harmonic function representing the external influence is completely and uniquely defined by boundary conditions. Since the *internal influence* is already uniquely defined by f , when appropriate boundary conditions are given, ϕ (the solution to (1)) is uniquely defined.

4.1.1 Green's Function

One approach to solve the Poisson and Laplace equations uses an integral kernel called the *Green's function*, $G(\mathbf{x}, \mathbf{x}_0)$.

The Green's function is defined as the potential created at \mathbf{x}_0 due to an impulse (energy) source represented by the *Dirac delta function* located at \mathbf{x} , (as shown in Fig. 3), i.e., it is the solution to the equation

$$\nabla^2 G(\mathbf{x}, \mathbf{x}_0) = \delta(\mathbf{x} - \mathbf{x}_0).$$

In the case of a single source located at \mathbf{x} in an infinite domain, it is also called the *free-space Green's function*, $G_\infty = G_\infty(\mathbf{x}, \mathbf{x}_0)$, and is given as

$$\begin{aligned} G_\infty(\mathbf{x}, \mathbf{x}_0) &= \frac{1}{2\pi} \log(|\mathbf{x} - \mathbf{x}_0|) & \mathbf{x}, \mathbf{x}_0 \in \mathbb{R}^2, \\ G_\infty(\mathbf{x}, \mathbf{x}_0) &= -\frac{1}{4\pi|\mathbf{x} - \mathbf{x}_0|} & \mathbf{x}, \mathbf{x}_0 \in \mathbb{R}^3. \end{aligned} \tag{3}$$

According to the *sifting property* of the Dirac delta function, any continuous source function can be represented as a collection of infinitely many impulse sources, as

$$f(\mathbf{x}_0) = \int_{\mathbb{R}^n} f(\mathbf{x}) \delta(\mathbf{x} - \mathbf{x}_0) \, d\mathbf{x}.$$

Then, the Poisson equation $\nabla^2 \phi = f$ on \mathbb{R}^n , with $f(\mathbf{x}) \rightarrow 0$ for $\mathbf{x} \rightarrow \infty$ can be solved [39] as

$$\phi(\mathbf{x}_0) = \int_{\mathbb{R}^n} G_\infty(\mathbf{x}, \mathbf{x}_0) f(\mathbf{x}) \, d\mathbf{x}. \tag{4}$$

The above *integral solution* computes the potential ϕ at a point $\mathbf{x}_0 \in \mathbb{R}^n$ due to the sources defined by f at all $\mathbf{x} \in \mathbb{R}^n$. However, given a bounded domain $\Omega \subset \mathbb{R}^n$, the computation of ϕ using (4) can be split into two parts – inside Ω and outside Ω .

$$\phi(\mathbf{x}_0) = \int_{\Omega} G_\infty f(\mathbf{x}) \, d\mathbf{x} + \int_{\mathbb{R}^n/\Omega} G_\infty f(\mathbf{x}) \, d\mathbf{x}. \tag{5}$$

From the discussion presented above, it is known that the second integral ($\int_{\mathbb{R}^n/\Omega} \dots$) creates a harmonic potential in Ω , whereas the first integral ($\int_{\Omega} \dots$) leads to a non-harmonic potential in Ω . Section 5.1 will elaborate on how to make use of this insight for computing the HHD without assuming boundary conditions. However, next, the traditional way to compute the potential functions on bounded domains using boundary conditions is discussed.

4.1.2 Boundary Conditions

As already discussed, for bounded domains, a unique solution of the Poisson equation (1) is obtained by imposing boundary conditions. Two common types of boundary conditions are (a) *Dirichlet*, which specifies the value of ϕ at the boundary $\partial\Omega$, i.e., $\phi = g$ on $\partial\Omega$; and (b) *Neumann*, which specifies the value of the derivative of ϕ with respect to the boundary, i.e., $\frac{\partial\phi}{\partial\vec{n}} = h$ on $\partial\Omega$, where, \vec{n} is the exterior normal to the boundary.

To compute ϕ for a bounded domain Ω using the integral solution, one typically uses the *finite-space Green's function* G_Ω , which is influenced by both the domain Ω and its

boundary $\partial\Omega$. In this case, the Poisson equation (1) can be solved [39] as

$$\phi(\mathbf{x}_0) = \int_{\Omega} G_{\Omega} f(\mathbf{x}) \, d\mathbf{x} + \oint_{\partial\Omega} \phi(\mathbf{x}) \frac{\partial G_{\Omega}}{\partial \vec{n}} \, d\mathbf{x} - \oint_{\partial\Omega} G_{\Omega} \frac{\partial \phi(\mathbf{x})}{\partial \vec{n}} \, d\mathbf{x}.$$

In the case of Dirichlet boundary conditions, one typically finds a G_{Ω} that vanishes at the boundary, such that the third integral becomes zero. On the other hand, for Neumann boundary conditions, one imposes $\frac{\partial G_{\Omega}(\mathbf{x}, \mathbf{x}_0)}{\partial \vec{n}} = 1/(\oint_{\partial\Omega} d\mathbf{x})$, in which case the second integral becomes a constant. In general, however, computing the Green's function for an arbitrary domain is non-trivial, and typically, it is not available in closed-form.

With an understanding of the Poisson equation and potential functions, we now discuss the fundamental equations governing the HHD.

4.2 The Helmholtz-Hodge Decomposition

The Helmholtz-Hodge decomposition [7] decomposes a vector field into rotation-free, divergence-free, and harmonic vector fields. Consider a smooth vector field $\vec{\xi} : \Omega \rightarrow \mathbb{R}^n$, where $\Omega \subseteq \mathbb{R}^n$ (for $n = 2, 3$), then

$$\vec{\xi} = \vec{d} + \vec{r} + \vec{h}, \quad (6)$$

where, \vec{d} is rotation-free ($\nabla \times \vec{d} = \vec{0}$), \vec{r} is divergence-free ($\nabla \cdot \vec{r} = 0$), and \vec{h} is harmonic ($\nabla \times \vec{h} = \vec{0}$ and $\nabla \cdot \vec{h} = 0$). This leads to the following equalities:

$$\begin{aligned} \nabla \cdot \vec{d} &= \nabla \cdot \vec{\xi}, \\ \nabla \times \vec{r} &= \nabla \times \vec{\xi}. \end{aligned} \quad (7)$$

Notice that this system of equations is under-specified, since for any harmonic flows \vec{h}_d and \vec{h}_r , the following fields also represent a valid HHD: $\vec{d}' = \vec{d} + \vec{h}_d$, $\vec{r}' = \vec{r} + \vec{h}_r$, and $\vec{h}' = \vec{h} - \vec{h}_d - \vec{h}_r$. For infinite space ($\Omega = \mathbb{R}^n$) where $\vec{\xi}$ goes to zero at infinity, no harmonic flow can exist ($\vec{h}_d = \vec{h}_r = \vec{h} = \vec{h}' = \vec{0}$), and thus the decomposition is unique. However, for domains with boundary, or for non-simply connected domains, a harmonic flow may exist leading to a non-trivial solution space. The traditional way to obtain a unique solution is to specify a set of boundary conditions, which effectively determine \vec{h}_d and \vec{h}_r , and thus choose a particular solution from the space of valid decompositions satisfying (7).

While there exist several boundary conditions motivated by a variety of applications and spatial discretizations, the most common boundary conditions found in literature [25], [26], [40] are the *normal-parallel (NP)* boundary conditions, which impose the rotation-free and the divergence-free flows to be normal and parallel to the boundary, respectively. Using the NP boundary conditions, the HHD_(NP) is defined as

$$\vec{\xi} = \vec{d}_{(NP)} + \vec{r}_{(NP)} + \vec{h}_{(NP)},$$

such that $\vec{d}_{(NP)} \times \vec{n} = 0$ and $\vec{r}_{(NP)} \cdot \vec{n} = 0$. In addition to uniqueness, these boundary conditions maintain L^2 orthogonality between \vec{d} and \vec{r} , by ensuring that $\int_{\Omega} \vec{d} \cdot \vec{r} \, dV = 0$. The particular issue of orthogonality will be discussed in more detail in Section 5.

4.2.1 The HHD as Poisson Equations

To compute the decomposition, the components \vec{d} and \vec{r} are represented as the gradient of a scalar potential D , and the curl of a vector potential \vec{R} , respectively. Substituting $\vec{d} = \nabla D$ and $\vec{r} = \nabla \times \vec{R}$ in (7), we get two Poisson equations,

$$\begin{aligned} \Delta D &= \nabla \cdot \vec{\xi}, \\ \Delta \vec{R} &= -\nabla \times \vec{\xi}, \end{aligned} \quad (8)$$

where, Δ is the (scalar) Laplacian, i.e., $\Delta = \nabla^2$, and $\vec{\Delta}$ is the vector Laplacian, i.e., $\vec{\Delta} = (\nabla \nabla \cdot) - (\nabla \times \nabla \times)$. Furthermore, due to the gauge condition [22], [41], $\nabla \cdot \vec{r} = 0$ implies $\nabla \cdot \vec{R} = 0$. Thus, $\vec{\Delta} \vec{R} = -\nabla \times \nabla \times \vec{R}$. The Poisson equations (8) are solved, leading to the components \vec{d} and \vec{r} , and then, the harmonic component is computed as the remainder: $\vec{h} = \vec{\xi} - \vec{d} - \vec{r}$.

In two-dimensions, the curl can be represented as a scalar value in the normal direction to the domain. This leads to a simpler representation of \vec{r} as the co-gradient of a scalar potential R , i.e., $\vec{r} = J \nabla R$, where J is the $\pi/2$ -rotation operator. Consequently, the second Poisson equation in (8) can be simplified as

$$\Delta R = -\nabla \cdot J \vec{\xi}. \quad (9)$$

4.2.2 The Artifacts of the NP Boundary Conditions

To uniquely define the potentials $D_{(NP)}$ and $\vec{R}_{(NP)}$ using the NP boundary conditions, the Poisson equations (8) are solved by setting $D_{(NP)} = 0$ and $\vec{R}_{(NP)} = \vec{0}$ on the boundary. We only discuss the computation of $D_{(NP)}$, since the computation of $\vec{R}_{(NP)}$ follows similar arguments. Using the superposition principle, one can represent $D_{(NP)} = D^* + H_d$, such that

$$\begin{aligned} \nabla^2 D^* &= \nabla \cdot \vec{\xi} & \text{and} & & \nabla^2 H_d &= 0 & \text{in } \partial\Omega, \\ D^* &= g & & & H_d &= -g & \text{on } \partial\Omega, \end{aligned}$$

where, D^* is the divergent potential that captures all the divergence of $\vec{\xi}$, and g is the distribution of D^* on the boundary. As already discussed, g is usually not known, and therefore, by solving for $D_{(NP)}$, one adds a harmonic function H_d which has the values $-g$ on the boundary. Thus, a harmonic flow $\vec{h}_d = \nabla H_d$ is added to $\vec{d}_{(NP)}$.

To illustrate the artifacts due to imposing zero potential on the boundary, we refer to Fig. 1 which shows an extreme but not an uncommon scenario. Moreover, observe the third row in Fig. 6 which shows that due to the imposed normal flow in $\vec{d}_{(NP)}$, the flow disagrees substantially from the known analytical flow, \vec{d}_{known} .

5 THE NATURAL HHD

To understand the internal influence for a given domain, we recall from the theory of potential functions and energy sources, that every point (inside and outside the domain) with a non-zero energy source creates a potential. In this context, the divergence and rotation fields can be seen as a collection of impulse sources for divergent and rotational potentials, such that every point (inside and outside the domain) with a non-zero divergence and rotation influences

the divergent and rotational flows respectively. Further, recall that harmonic potentials represent the external influence. We use these intuitions of internal and external influences to formally define the natural HHD.

Definition 5.1 (The Natural HHD). *The natural Helmholtz-Hodge decomposition, HHD^* : $\vec{\xi} = \vec{d}^* + \vec{r}^* + \vec{h}^*$, is obtained by separating the flows due to internal and external influences, such that the natural divergent (\vec{d}^*) and natural rotational (\vec{r}^*) components represent the flows influenced by the divergence and rotation of $\vec{\xi}$ inside the domain. Consequently, the natural harmonic component (\vec{h}^*) is the flow influenced only by the exterior (boundary) of the domain.*

5.1 Construction and Uniqueness

Given a smooth n -dimensional vector field $\vec{\xi} : \Omega \rightarrow \mathbb{R}^n$ for $n = 2, 3$, where Ω is a bounded subset of \mathbb{R}^n , the goal is to interpret and compute the natural components of $\vec{\xi}$. Using $\vec{\xi}$, we define another smooth vector field on infinite space, $\vec{V} : \mathbb{R}^n \rightarrow \mathbb{R}^n$ such that

- $\vec{V}(\mathbf{x}) = \vec{\xi}(\mathbf{x})$ for all $\mathbf{x} \in \Omega$, and
- $|\vec{V}(\mathbf{x})| \rightarrow 0$ for $|\mathbf{x}| \rightarrow \infty$.

By definition, \vec{V} captures the properties of $\vec{\xi}$ in Ω , i.e., $\nabla \cdot \vec{V} = \nabla \cdot \vec{\xi}$ and $\nabla \times \vec{V} = \nabla \times \vec{\xi}$ in Ω , and also provides a smooth flow on \mathbb{R}^n that vanishes at infinity.

In order to compute the natural HHD of $\vec{\xi}$, we first study the HHD of \vec{V} . This indirect approach of using \vec{V} has two main advantages: 1) the HHD of \vec{V} is unique by definition, since it does not contain a harmonic component, and 2) it allows the use of the free-space Green's function G_∞ which is trivially defined in closed form. The HHD of \vec{V} is

$$\vec{V} = \nabla D + \nabla \times \vec{R},$$

where, the potentials D and \vec{R} are computed by solving the following Poisson equations.

$$\begin{aligned} \Delta D &= \nabla \cdot \vec{V} && \text{in } \mathbb{R}^n, \\ \Delta \vec{R} &= -\nabla \times \vec{V} && \text{in } \mathbb{R}^n. \end{aligned}$$

Using G_∞ , D and \vec{R} can be computed as

$$\begin{aligned} D(\mathbf{x}_0) &= \int_{\mathbb{R}^n} G_\infty \nabla \cdot \vec{V}(\mathbf{x}) \, d\mathbf{x} && \mathbf{x}, \mathbf{x}_0 \in \mathbb{R}^n, \\ \vec{R}(\mathbf{x}_0) &= - \int_{\mathbb{R}^n} G_\infty \nabla \times \vec{V}(\mathbf{x}) \, d\mathbf{x} && \mathbf{x}, \mathbf{x}_0 \in \mathbb{R}^n. \end{aligned}$$

Similar to (5), these expressions can be split into two parts—inside Ω and outside Ω . Furthermore, since $\nabla \cdot \vec{V}(\mathbf{x}) = \nabla \cdot \vec{\xi}(\mathbf{x})$ and $\nabla \times \vec{V}(\mathbf{x}) = \nabla \times \vec{\xi}(\mathbf{x})$ for $\mathbf{x} \in \Omega$, we have

$$\begin{aligned} D(\mathbf{x}_0) &= \int_{\Omega} G_\infty \nabla \cdot \vec{\xi}(\mathbf{x}) \, d\mathbf{x} + \int_{\mathbb{R}^n/\Omega} G_\infty \nabla \cdot \vec{V}(\mathbf{x}) \, d\mathbf{x}, \\ \vec{R}(\mathbf{x}_0) &= - \int_{\Omega} G_\infty \nabla \times \vec{\xi}(\mathbf{x}) \, d\mathbf{x} - \int_{\mathbb{R}^n/\Omega} G_\infty \nabla \times \vec{V}(\mathbf{x}) \, d\mathbf{x}, \end{aligned}$$

where, \int_{Ω} and $\int_{\mathbb{R}^n/\Omega}$ represent the influence of the interior and the exterior with respect to Ω respectively.

Note that D and \vec{R} are defined over \mathbb{R}^n , however, since the final goal is to compute the natural HHD of $\vec{\xi}$ in Ω , we restrict these expressions to $\mathbf{x}_0 \in \Omega$. Since, by definition, the natural potentials represent only the internal influence,

the following expressions provide formal definitions to the natural potentials.

$$\begin{aligned} D^*(\mathbf{x}_0) &= \int_{\Omega} G_\infty \nabla \cdot \vec{\xi}(\mathbf{x}) \, d\mathbf{x} && \mathbf{x}, \mathbf{x}_0 \in \Omega, \\ \vec{R}^*(\mathbf{x}_0) &= - \int_{\Omega} G_\infty \nabla \times \vec{\xi}(\mathbf{x}) \, d\mathbf{x} && \mathbf{x}, \mathbf{x}_0 \in \Omega. \end{aligned} \tag{10}$$

From Section 4.1, we know that the integral $\int_{\Omega}(\dots)$ defines a non-harmonic potential inside Ω . On the other hand, the integral $\int_{\mathbb{R}^n/\Omega}(\dots)$ defines a harmonic potential in Ω . Therefore, ignoring the latter does not change the divergence and rotation captured by the non-harmonic potentials. As a result, the natural components $\vec{d}^* = \nabla D^*$ and $\vec{r}^* = \nabla \times \vec{R}^*$ match the divergence and rotation of $\vec{\xi}$. Consequently, the natural harmonic component, computed as the remainder $\vec{h}^* = \vec{\xi} - \vec{d}^* - \vec{r}^*$, is both divergence- and rotation-free. Finally, note that the natural potentials D^* and \vec{R}^* are uniquely determined by (10), and therefore, so are \vec{d}^* , \vec{r}^* , and \vec{h}^* . Hence, the natural HHD is unique.

Theorem 5.2. *Given a vector field $\vec{\xi}$ on a bounded domain Ω , its natural Helmholtz-Hodge decomposition as defined by Definition 5.1 is unique.*

The significance of the natural HHD is that the uniqueness can be obtained without assuming any boundary conditions on D^* and \vec{R}^* .

Interpretation of the Natural Harmonic Flow. From the discussion so far, we know that the HHD of \vec{V} is unique, and is given by

$$\begin{aligned} \vec{V}(\mathbf{x}_0) &= \nabla D^*(\mathbf{x}_0) + \nabla \int_{\mathbb{R}^n/\Omega} G_\infty \nabla \cdot \vec{V}(\mathbf{x}) \, d\mathbf{x} \\ &\quad + \nabla \times \vec{R}^*(\mathbf{x}_0) - \nabla \times \int_{\mathbb{R}^n/\Omega} G_\infty \nabla \times \vec{V}(\mathbf{x}) \, d\mathbf{x}, \end{aligned}$$

where, $\mathbf{x}_0 \in \mathbb{R}^n$. On the other hand, the natural HHD of $\vec{\xi}$ is given by

$$\vec{\xi}(\mathbf{x}_0) = \nabla D^*(\mathbf{x}_0) + \nabla \times \vec{R}^*(\mathbf{x}_0) + \vec{h}^*,$$

where, $\mathbf{x}_0 \in \Omega$. By definition, $\vec{V}(\mathbf{x}_0) = \vec{\xi}(\mathbf{x}_0)$ for all $\mathbf{x}_0 \in \Omega$. As a result, for all $\mathbf{x}_0 \in \Omega$, we have

$$\begin{aligned} \vec{h}^*(\mathbf{x}_0) &= \nabla \int_{\mathbb{R}^n/\Omega} G_\infty \nabla \cdot \vec{V}(\mathbf{x}) \, d\mathbf{x} \\ &\quad - \nabla \times \int_{\mathbb{R}^n/\Omega} G_\infty \nabla \times \vec{V}(\mathbf{x}) \, d\mathbf{x} && \mathbf{x} \in \mathbb{R}^n. \end{aligned}$$

This means that the natural harmonic component of $\vec{\xi}$ can be constructed using the divergence and curl of a hypothetical flow on \mathbb{R}^n . There can exist many such flows leading to the same \vec{h}^* . This degree of freedom matches our understanding of harmonic flow that its unique definition requires knowledge about the exterior. However, using the proposed internal-external split, one does not need to find a particular \vec{V} , but instead, can determine the influence of the unknown in a data-driven manner. As expected, for computation of \vec{d}^* and \vec{r}^* , no information about the exterior (or the boundary) is needed, and therefore, the indirect approach to consider an infinite vector field is only a thought experiment.

5.2 Advantages and Limitations

Computing the natural components by distinguishing between the internal and external influences has several advantages. First, computation of the natural HHD depends only upon the flow inside the domain, and not on the relative alignment of the flow with its boundary. Notice that this approach also works for non-simply connected subsets of \mathbb{R}^n (cf. Fig. 6).

Second, due to the conceptual domain extension to \mathbb{R}^n one can utilize the free-space Green's function G_∞ , which is simple and known in closed-form. Therefore, the computation on bounded domains can bypass the step of computing the finite-space Green's function G_Ω which is much more involved, since it may not be known in closed-form for the given domain. Third, one could think of using a similar idea of extending the domain for existing techniques in order to reduce boundary artifacts. However, being global in nature, such techniques would depend upon the flow in the extended domain. On the other hand, the proposed approach is oblivious to how the field is completed in the extended domain, and does not depend upon the size and shape of the extended domain.

Finally, unlike the other techniques which use boundary conditions to obtain uniqueness, the computation of the natural HHD does not assume a decomposition of the boundary flow. Therefore, the fidelity of the flow is not compromised, and the components obtain the most "natural" values on the boundary.

The only limitation of the natural HHD is that it is not guaranteed to be L_2 -orthogonal. However, orthogonality between the incompressible and irrotational components is important only for certain applications in fluid simulation, as it helps decouple the errors in the two components. For applications in visualization and analysis, orthogonality is not required. Instead, we seek more desirable properties like flow topology, which can be attributed to the interior and exterior of the domain. Therefore, we believe that the natural HHD is suited to most applications in such areas.

5.3 Local Computation and Local Approximation

Besides the conceptual advantages of the natural HHD described above, it has some important practical benefits. The natural HHD is computed point-wise, and does not assume any boundary conditions. Consequently, considering a smaller area of interest $\Omega_1 \subset \Omega$, it is possible to obtain a *local decomposition* in Ω_1 by restricting the computation to Ω_1 . Physically, this means that we can compute the components in a smaller Ω_1 influenced by the divergence and rotation in the larger Ω . In contrast, using the state-of-the-art techniques [25], [26], [27], [28], which are global solutions, it is not possible to compute a local decomposition using global information.

Furthermore, it is also possible to obtain a *local approximation* to the global natural HHD by ignoring the flow outside Ω_1 . This computes the component flows inside Ω_1 due to the influence of Ω_1 instead of Ω . The error of this approximation is then given by the ignored term: $\int_{\Omega/\Omega_1} G_\infty(\dots)$.

However, in practice, this error is often negligible for two reasons. First, for turbulent flows, the external influences, e.g., positive/negative divergences and clockwise/

counterclockwise rotations often cancel each other. Second, since the Green's function is a distance-based weighting function whose value goes to zero as the distance increases, for suitably chosen finite $\Omega_1 \subset \Omega$, it can be ignored for points in Ω/Ω_1 .

Both the local computation as well as the local approximation play crucial roles in terms of reducing computational costs, especially when Ω_1 is much smaller than Ω , as illustrated in Section 7.

5.4 Quantifying the Harmonic Flow

Although harmonic flows are well studied, currently there exist no techniques to determine whether a given flow on a given domain "contains" a harmonic piece or not. Since harmonic is most commonly defined as the flow that is both divergence- and rotation-free, at best, one can only evaluate if the given flow is rotation-free, divergence-free, or both (harmonic).

However, an earlier ignored, but an important property of harmonic flows is that they are caused by influences that are external to the given domain. Utilizing this property, the internal-external split proposed in this paper computes the harmonic flow indirectly. This allows us to, for the first time, answer an important question "*Given a vector field $\vec{\xi}$ defined on Ω , how much harmonic flow does it contain?*".

For a given flow $\vec{\xi}$ on Ω , its non-harmonic component, denoted as \vec{v}^* , can be computed using its divergence and rotation: $\vec{v}^* = (\nabla \int_\Omega G_\infty \nabla \cdot \vec{\xi} \, dx) + (\nabla \times \int_\Omega G_\infty \nabla \times \vec{\xi} \, dx)$, and quantified using a vector norm μ that maps the space of vector fields to positive real numbers. By definition, μ must satisfy three properties: (1) $\mu(\vec{a}) \geq 0$; (2) $\mu(\vec{a}) = 0$ if and only if $\vec{a} = \vec{0}$; and (3) $\mu(\vec{a} + \vec{b}) \leq \mu(\vec{a}) + \mu(\vec{b})$.

Owing to the fact that the non-harmonic component \vec{v}^* is guaranteed to not contain any external influences (harmonic), we can quantify the amount of harmonic flow present in $\vec{\xi}$ indirectly. In particular, since $\vec{\xi} = \vec{v}^* + \vec{h}^*$, it follows that $\mu(\vec{\xi}) \leq \mu(\vec{v}^*) + \mu(\vec{h}^*)$. Using this expression, the lower bound on the norm of harmonic flow present in $\vec{\xi}$ with respect to Ω is $\mu(\vec{h}^*) \geq \mu(\vec{\xi}) - \mu(\vec{v}^*)$, where, both the terms in the RHS of this inequality can be uniquely determined.

In summary, the harmonic flow (external influences) present in a given flow can be quantified using a user-defined norm, such as the L_2 norm. The metric will be zero if and only if there are no external influences, and $\vec{\xi}$ can be uniquely decomposed into two natural non-harmonic components. On the other hand, a non-zero metric indicates that $\vec{\xi}$ is not directly useful to study internal features, and the natural HHD must be used to first dissociate the harmonic component. This quantification can also serve as a benchmark for different HHDs to assess the quality of the resulting components and their usability in applications requiring open boundary.

6 IMPLEMENTATION DETAILS

The computation of the natural HHD as the integral solution of the Poisson equation using the free space Green's function requires (a) computation of the divergence, curl, and gradients; and (b) integration of the results over the given domain. For both these steps any appropriate

discretization can be used. For clarity of the presentation, we limit our discussion to 2D, with bilinear vector fields on regular grids, and PC vector fields on triangulated domains. However, all concepts trivially extend to 3D and other interpolants.

In the following, let \mathcal{T} represent a triangulated domain where the PC vector field is defined on the faces, and all scalar quantities are defined on the vertices, and \mathcal{G} be a regular grid of size $[X \times Y]$, and grid spacings dx and dy , where all quantities (including the vector field) are defined on the vertices.

Computation of divergence, curl, and gradient. To define the differential operators on \mathcal{G} , we compute the partial derivatives in each dimension using central finite differences for the interior nodes, and forward/backward finite differences for boundary nodes. Using these partial derivatives we can obtain the discrete approximations to the divergence, curl, and gradient operators.

For PC vector fields on \mathcal{T} , we use the finite element framework proposed by Polthier and Preuß [25]. The divergence (and curl) at a vertex is computed as the sum of dot products of the vector field with the normal (and tangent) along the boundary of the one-ring neighborhood of the vertex. The gradient of a scalar field defined at vertices of \mathcal{T} is a vector field defined at its faces. For each face, it is the sum of the gradient of its barycentric coordinates weighted by the function value at the corresponding vertices.

Integration over the domain. Let C , E , and I be the set of vertices at the four corners, at the boundary (not including the corners), and the interior of \mathcal{G} . Then, the integral of a function f over \mathcal{G} can be computed by applying the 1D trapezoidal method over the x -dimension, and subsequently over the y -dimension. This gives the following expression $\int_{\mathcal{G}} f(x, y) \approx \frac{dx \, dy}{4} (\sum_{v \in C} f_v + 2 \sum_{v \in E} f_v + 4 \sum_{v \in I} f_v)$, where, f_v is the value of f at the vertex v .

On the other hand, for every vertex $v \in \mathcal{T}$, let $\text{Area}(v)$ denote the area of the corresponding cell in the Voronoi dual mesh (obtained by connecting the centroids of the triangles in \mathcal{T}). Then, the integral of a function over the domain is computed as $\int_{\mathcal{T}} f(x, y) \approx \sum_{v \in \mathcal{T}} f_v \text{Area}(v)$.

Using the modules defined above, the integral solutions is computed as weighted sum over all the vertices, making it an $O(n^2)$ algorithm, where n is the number of vertices in \mathcal{T} or \mathcal{G} . However, the technique is trivially parallelizable since once the divergence and rotation are available, computation at every vertex can be performed independently and in parallel.

7 EVALUATION AND RESULTS

This section provides results of our technique applied to some synthetic and simulated data sets. The aim is to first evaluate the accuracy and stability of the technique by comparing it with the known component fields, and then to demonstrate its versatility and robustness by applying it to different physical flows. For comparisons, we use the LS-FEM technique of Polthier and Preuß [25] as the representative of $\text{HHD}_{(\text{NP})}$, i.e., the HHD with NP boundary conditions ($\vec{d}_{(\text{NP})} \times \vec{n} = 0$ and $\vec{r}_{(\text{NP})} \cdot \vec{n} = 0$). Note that the majority of the differences among the two approaches are due to the

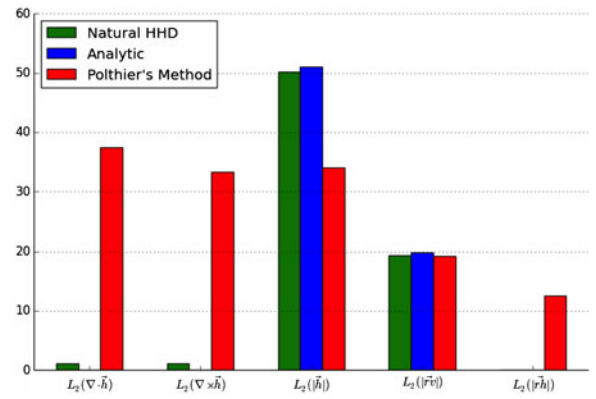


Fig. 4. Quantitative comparison shows that the natural components approximate the analytic fields better.

choice of boundary conditions, and not how the solution is computed. The visualizations in this sections are created using line integral convolution (LIC) [42], color-mapped to represent vector magnitudes, where purple-white represent low-high values.

7.1 Comparisons with Analytical Fields

We analytically create a divergent, \vec{d}_{known} , a rotational, \vec{r}_{known} , and a translational (harmonic), \vec{h}_{known} flow, and add them to construct a synthetic test case, $\vec{\xi} = \vec{d}_{\text{known}} + \vec{r}_{\text{known}} + \vec{h}_{\text{known}}$ as described and illustrated in Fig. 5b. Similar to the example given by Wiebel (cf. Fig. 1), this field is contrived to represent a scenario of open boundary, and as a result, the standard boundary conditions would be incompatible.

The “ideal” HHD of $\vec{\xi}$ should recover the three input ingredients accurately. However, as expected, the components of $\text{HHD}_{(\text{NP})}$ (see Fig. 5a) show artifacts near the boundary. In particular, notice that the flow magnitudes are near-zero for both $\vec{d}_{(\text{NP})}$ and $\vec{r}_{(\text{NP})}$ near the corners of the domain, and the critical points in the rotational and divergent flows are shifted inwards. Furthermore, the corresponding harmonic flow $\vec{h}_{(\text{NP})}$ does not reflect the added translation \vec{h}_{known} . In comparison, the components of the natural HHD (cf. Fig. 5c) are virtually indistinguishable from the analytic components.

Since \vec{d} and \vec{r} are computed as gradient and curl of the corresponding potentials, their numerical divergence and rotation are always zero. Therefore, the divergence and rotation present in \vec{h} is a good indicator of the numerical quality of the decomposition. As shown by the first two sets of columns in Fig. 4, our results closely match the expected results, while the results of $\text{HHD}_{(\text{NP})}$ show large deviations. To further compare the two decompositions, we quantify the amount of external influences in the corresponding components. The third set of columns shows the L_2 norm for $|\vec{h}^*|$, $|\vec{h}_{\text{known}}|$, and $|\vec{h}_{(\text{NP})}|$, and indicates that our solution extracts almost all of the harmonic flow into \vec{h}^* . The last two sets of columns show the amounts of non-harmonic and harmonic flows present in the obtained divergence-free fields, denoted as \vec{r}^{div} and \vec{r}^{rot} . The three columns for \vec{r}^{div} almost match, meaning that the net amount of rotational flow is conserved in all the rotational components. However, there exists a large amount of harmonic flow in $\vec{r}_{(\text{NP})}$. In contrast, the harmonic flow contained in \vec{r}^{rot} is unnoticeable. The results on the obtained rotation-free

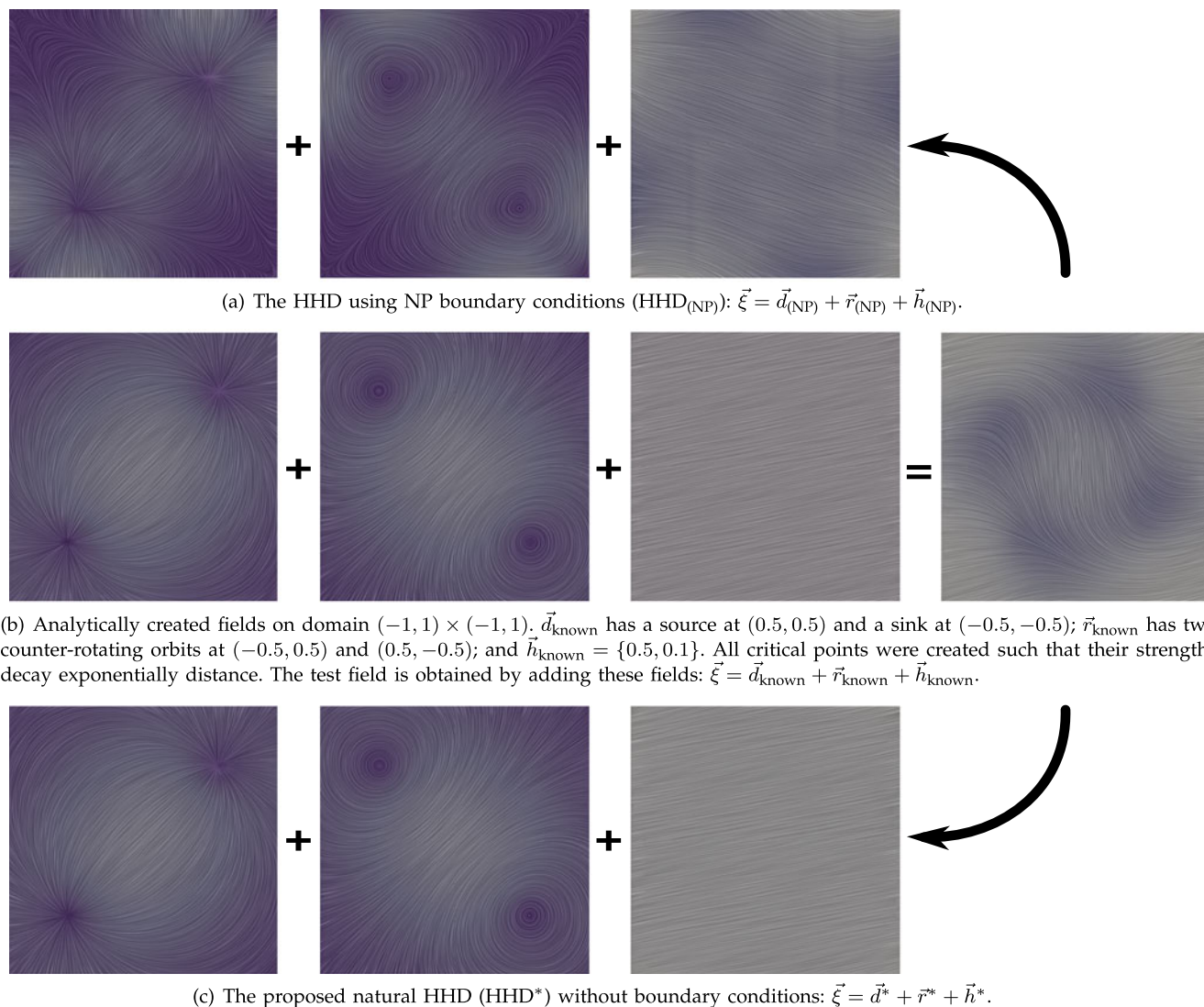


Fig. 5. Comparison of the natural HHD (bottom) and Polthier's LS-FEM [25] with NP boundary conditions (top) with the analytic flows (middle). The results of natural HHD are much closer to the ground truth.

fields (not shown in the figure) follow a similar trend. These quantitative comparisons corroborate the visual impression that HHD* recovers the known solution significantly better than HHD_(NP), whose results are not useful for applications requiring open boundary.

Fig. 6 shows the results of an experiment where we sampled an analytical flow ($\vec{\xi} = \vec{d}_{\text{known}} + \vec{h}_{\text{known}}$) on a regular grid, a rotated regular grid, and an unstructured annulus mesh. Comparing the flows, one can observe that our results match more closely to the analytical flow. In particular, the fields \vec{d}^* and \vec{h}^* reflect the best estimates of \vec{d}_{known} and \vec{h}_{known} , given the data inside the domain. On the other hand, $\vec{d}_{(NP)}$ and $\vec{h}_{(NP)}$ computed using NP boundary conditions impose boundary flow, and therefore show major deviations, especially near boundaries.

Stability. We further compare the stability of both techniques to sampling conditions and directions of the harmonic flow. First, we sample a rotating field on a fixed structured domain. As observed, the proposed approach is virtually invariant to the sampling while HHD_(NP) continuously forces alignment with the boundary causing significant

artifacts. In the second experiment, we continuously vary the direction of the added harmonic flow. As expected from Fig. 5, our solution remains unaffected while HHD_(NP) is only able to recover \vec{h}_{known} when it aligns with the boundary and produces significant global artifacts otherwise. The accompanying video, which can be found on the Computer Society Digital Library at <http://doi.ieeecomputersociety.org/10.1109/TVCG.2014.2312012> shows animations for both experiments.

7.2 Results on Physical Simulated Flows

Next, we apply our technique to different simulated flows reflecting a variety of physical phenomena. Notice that the results of Figs. 8, 11, and 12 show how physical flows do not conform with traditional boundary conditions, and thus existing techniques are not applicable.

Flow behind the cylinder and cuboid. The data shown in Fig. 7 is a single time-slice of a time-varying simulated flow. The flow is injected from the left boundary, and its behavior is observed behind the cylinder (on the left boundary of the

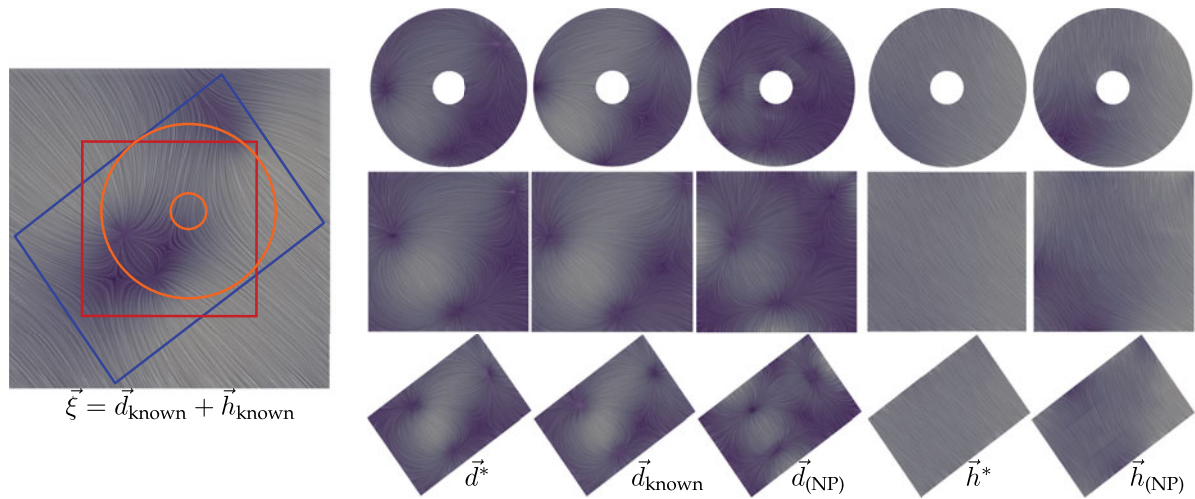


Fig. 6. The natural HHD (\vec{d}^* and \vec{h}^*) contains significantly fewer artifacts than the HHD with boundary conditions ($\vec{d}_{(NP)}$ and $\vec{h}_{(NP)}$) as compared to the true components— \vec{d}_{known} and \vec{h}_{known} (a translational flow $(1, -1)$, not shown).

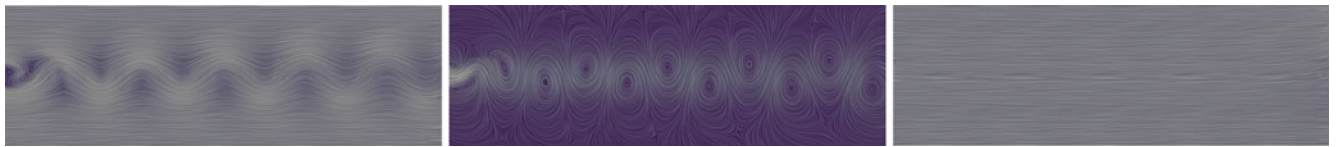


Fig. 7. The natural HHD of the flow behind the cylinder (left). \vec{r}^* reveals all vortices and is not aligned with the boundary (middle), while \vec{h}^* represents the background flow (right).

domain). As seen in the figure, our method extracts the harmonic components completely, and \vec{r}^* reveals the vortices. \vec{d}^* is zero since the original flow is incompressible. Note how \vec{r}^* is not aligned with either boundary – a result not feasible with traditional techniques. The computation of the natural HHD for this $[400 \times 50]$ data took about 1.06 seconds.

Fig. 10 shows the results of the natural HHD on a similar 3D flow. The data represents the flow behind a cuboid, where the flow is injected from one direction, and its behavior is observed behind the obstacle. Notice that \vec{r}^* reveals the vortical structures, while \vec{h}^* captures the background flow. The decomposition of this $[101 \times 101 \times 101]$ flow took about 120 seconds with 144 processes in parallel.

Lifted Ethylene Jet Flame. The second example is a direct numerical simulation of a turbulent lifted ethylene jet flame [5]. Unlike the previous data set, this is a compressible and highly turbulent flow. In this case, fuel is injected on the bottom of the domain creating a strong harmonic flow towards the top. Fig. 11 shows one snapshot for a 2D slice from the

center of the 3D flow. Both \vec{r}^* (Fig. 11b) and \vec{d}^* (Fig. 11c) are highly complex not aligned with the boundary and show some surprising structures. In particular, \vec{r}^* shows two global counter-rotating vortices rather than a streak of smaller vortices one may have expected. Finally, \vec{h}^* (Fig. 11d) reveals an elliptical shape reflecting the non-constant velocity profile imposed by the simulation. The decomposition of this $[800 \times 2,025]$ data took about 290 seconds with 144 processes in parallel.

Jet in cross-flow. The next data represents a simulation of a jet in cross-flow, which is a fundamental flow phenomenon in many engineering applications [17], [18], e.g., film cooling

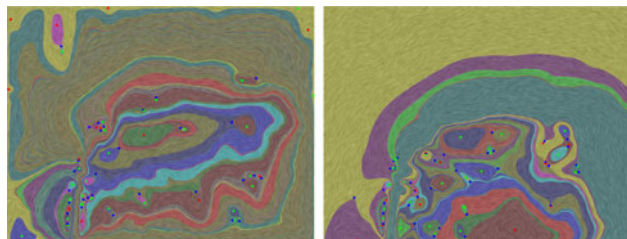


Fig. 8. Comparison of the topological decompositions of $\vec{r}_{(NP)}$ (left) and \vec{r}^* (right). Unphysical rotational structures are observed at the bottom-left and top-left corners in $\vec{r}_{(NP)}$ caused due to imposing parallel flow.

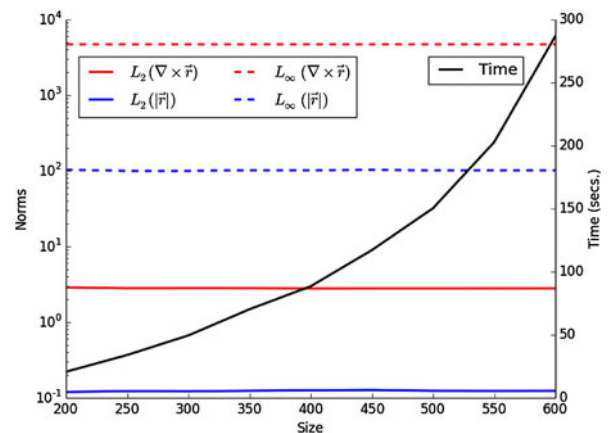


Fig. 9. Local computation for $\Omega_1 = \mathcal{G}_{200}$ using the data from $\Omega = \mathcal{G}_N$ with increasing N requires a quadratically increasing time (scaled to the right axis). On the other hand, the L_∞ and the normalized L_2 norms (log-scaled to the left axis) of $|\vec{r}|$ and $\nabla \times \vec{r}$ seem converged.

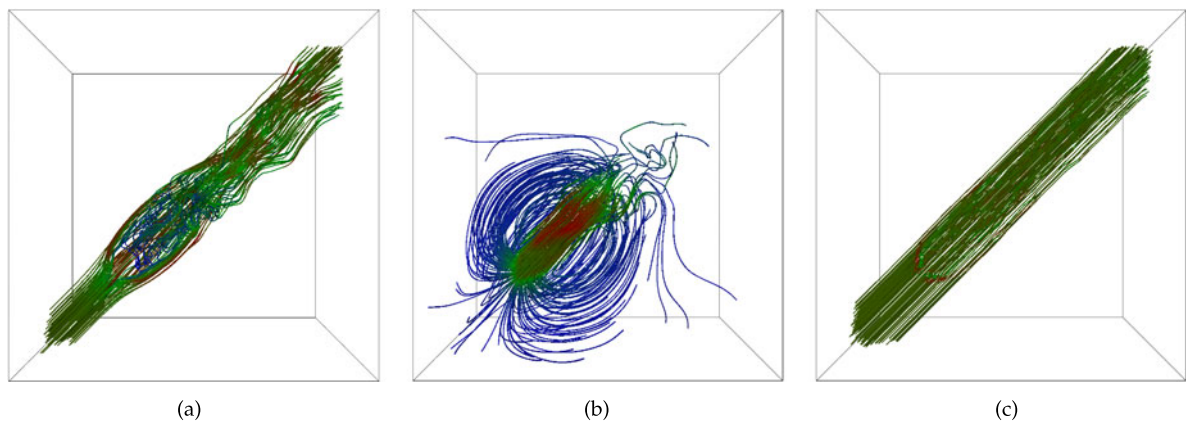


Fig. 10. The natural HHD of the flow behind cuboid (a). The figures show streamlines in the interesting regions. (b) \vec{r}^* reveals the vortical structures, and (c) \vec{h}^* shows the translation present in the flow (right).

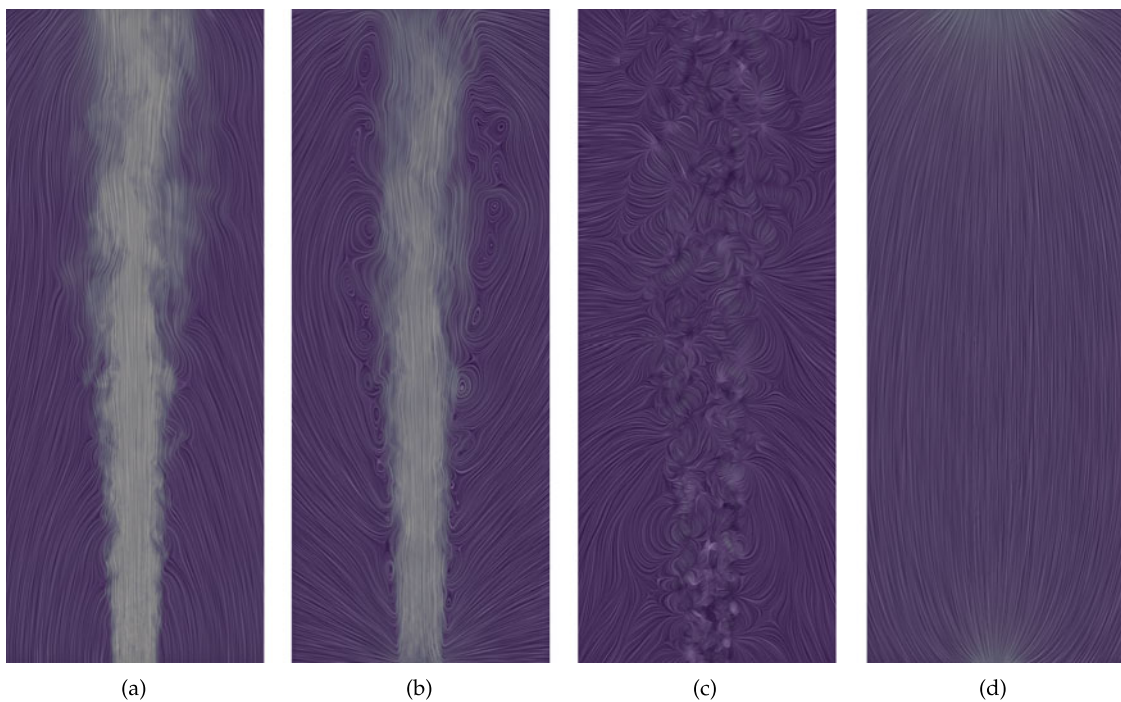


Fig. 11. (a) Flow in the center of a lifted ethylene jet flame [43]; (b) \vec{r}^* showing two global counter rotating vortices encapsulating smaller structures; (c) \vec{d}^* showing a large number of sources and sinks related to volume changes; and (d) \vec{h}^* computed as the residual showing an elliptical flow structure around the flame center.

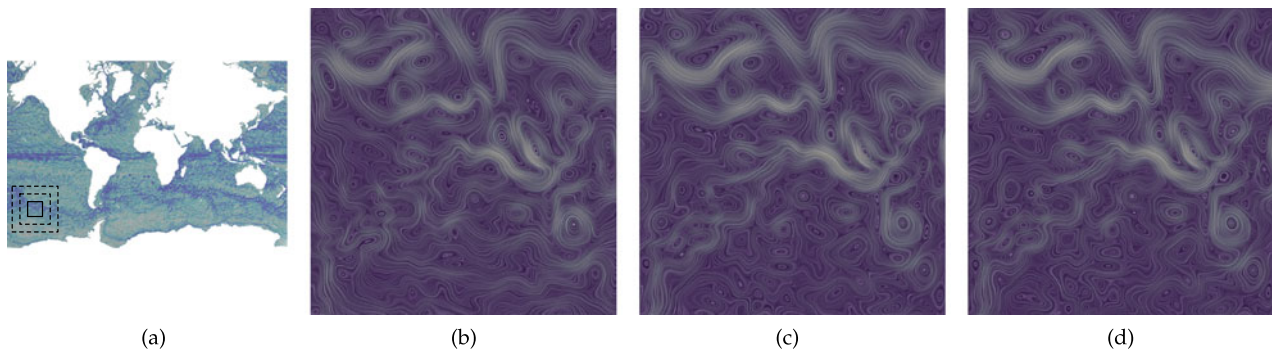


Fig. 12. Local approximation of \vec{r}^* in an ocean flow data set. The rotational fields are computed for the innermost tile, \mathcal{G}_{200} , shown in (a) by separately integrating over three concentric tiles (b) \mathcal{G}_{200} , (c) \mathcal{G}_{400} , and (d) \mathcal{G}_{600} .

of turbines, fuel injections, and dilution jets in gas-turbine combustors. The experimental set-up contains injection of flow through a jet at the bottom in the presence of a strong background transverse flow, the cross-flow.

To simplify the illustration, we take a 2D slice through the center of the 3D flow, such that the cross-flow is directed from left to right, and the jet can be seen at the bottom. Fig. 8 compares the rotational fields obtained through the $\text{HHD}_{(\text{NP})}$ and the natural HHD. We compute the critical points and the saddle separatrices of the flow to define its topological skeleton, which is then used to decompose the domain into non-overlapping regions. Since the topological decompositions of the two rotational fields are significantly different, the important question is which of these flows corresponds to the expected combustion phenomena. Through scientific insights of domain experts, we know that the small vortices near the top-left and bottom-left corners of $\vec{r}_{(\text{NP})}$ are unphysical, since the underlying physical model expects vortices to be generated behind the jet only. In summary, imposing parallel flow on the boundary produces false features (vortices) in the analysis.

Oceanic Currents. The final example is the surface flow taken from a 3D simulation of global ocean currents [1], as shown in Fig. 12, and we focus on a $\Omega_1 = [200 \times 200]$ region in the south Pacific ocean. To demonstrate the practical utility of the local computation and the local approximation of the natural HHD, we compute the decomposition for Ω_1 using the data from concentric grids $\Omega = \mathcal{G}_N$. Fig. 9 shows a quantitative comparison of the results when N is increased from 200 to 600. Note that while the time needed for the computation grows quadratically, the L_2 and L_∞ norms, and hence the decomposition already seems to have converged. As a result, in order to analyze the flow in Ω_1 , the natural HHD provides a local and faster technique, instead of using the existing global solutions, which would require the computation for the entire domain with over 5.3 million vertices. Fig. 12 shows the rotational flows obtained for $\Omega = \mathcal{G}_{200}$, $\Omega = \mathcal{G}_{400}$, and $\Omega = \mathcal{G}_{600}$.

8 DISCUSSION AND OUTLOOK

This paper presents the natural HHD as a new framework to compute a unique and non-orthogonal decomposition of a vector field based on internal and external influences, allowing for an open-boundary analysis. Our technique uses the integral solution of the Poisson equation, and decouples the decomposition from boundary conditions to avoid the typical boundary artifacts, and therefore produces significantly better results than state-of-the-art techniques. Furthermore, the decomposition can be computed locally, as well as in an approximate manner for faster, more targeted analysis of specific regions of interest. The proposed ideas allow, for the first time, to quantify the amount of harmonic flow in a given field. The computation of natural HHD opens new directions in support of various analysis techniques requiring independent study of internal and external influences.

Nevertheless, there remain some issues. The full decomposition is computationally expensive and new approaches are necessary to make it applicable to large-scale 3D data. Furthermore, although the proposed approach works for a

variety of spatial discretizations, it is limited to subsets of \mathbb{R}^n , and a similar approach for surfaces would be useful. Going forward, we hope that an easy to implement and reliable technique to compute the natural HHD will create new research interest in using it for various analysis tasks.

ACKNOWLEDGMENTS

The authors are grateful to Jacqueline Chen from the Sandia National Laboratory for the data used for Figs. 8 and 11. The data used in Fig. 7 has been simulated by Mahsa Mirzargar using Nektar++ [44], and the data in Fig. 10 by Alexander Wiebel using NaSt3DGP. The authors also thank Mathew Maltude from the Climate, Ocean and Sea Ice Modelling program at Los Alamos National Laboratory and the BER Office of Science UV-CDAT team for providing us access to the ocean data from Fig. 12. This work was performed under the auspices of the US Department of Energy (DOE) by Lawrence Livermore National Laboratory (LLNL) under contract DE-AC52-07NA27344. LLNL-JRNL-644755.

REFERENCES

- [1] M. Maltrud, F. Bryan, and S. Peacock, "Boundary impulse response functions in a century-long eddying global ocean simulation," *Environ. Fluid Mech.*, vol. 10, pp. 275–295, 2010.
- [2] S. A. Braun, M. T. Montgomery, and Z. Pu, "High-resolution simulation of hurricane bonnie (1998). Part I," *J. Atmospheric Sci.*, vol. 63, no. 1, pp. 19–42, 2006.
- [3] E. R. Hawkes, R. Sankaran, J. C. Sutherland, and J. H. Chen, "Scalar mixing in direct numerical simulations of temporally evolving plane jet flames with skeletal CO/H₂ kinetics," in *Proc. Combustion Inst.*, 2007, vol. 31, pp. 1633–1640.
- [4] C. S. Yoo, R. Sankaran, and J. H. Chen, "Three-dimensional direct numerical simulation of a turbulent lifted hydrogen jet flame in heated coflow: Flame stabilization and structure," *J. Fluid Mech.*, vol. 640, pp. 453–481, 2009.
- [5] C. S. Yoo, E. S. Richardson, R. Sankaran, and J. H. Chen, "A DNS study on the stabilization mechanism of a turbulent lifted ethylene jet flame in highly-heated coflow," *Proc. Combustion Inst.*, vol. 33, no. 1, pp. 1619–1627, 2011.
- [6] R. F. Stein and Å. Nordlund, "Realistic solar convection simulations," *Solar Phys.*, vol. 192, pp. 91–108, 2000.
- [7] H. Helmholtz, "Über Integrale der hydrodynamischen Gleichungen, welche den Wirbelbewegungen entsprechen," *J. für die reine und angewandte Mathematik*, vol. 1858, no. 55, pp. 25–55, Jan. 1858.
- [8] J. Helman and L. Hesselink, "Representation and display of vector field topology in fluid flow data sets," *IEEE Comput.*, vol. 22, no. 8, pp. 27–36, Aug. 1989.
- [9] A. Helgeland, B. A. P. Reif, Ø. Andreassen, and C. E. Wasberg, "Visualization of vorticity and vortices in wall-bounded turbulent flows," *IEEE Trans. Vis. Comput. Graph.*, vol. 13, no. 5, pp. 1055–1067, Sep./Oct. 2007.
- [10] F. Sadlo, R. Peikert, and E. Parkinson, "Vorticity based flow analysis and visualization for pelton turbine design optimization," in *Proc. IEEE Vis.*, 2004, pp. 179–186.
- [11] J. Hinkle, P. T. Fletcher, B. Wang, B. Salter, and S. Joshi, "4D MAP image reconstruction incorporating organ motion," in *Proc. 21st Int. Conf. Inform. Process. Med. Imag.*, 2009, pp. 676–687.
- [12] N. N. Mansour, A. Kosovichev, D. Georgobiani, A. Wray, and M. Miesch, "Turbulence convection and oscillations in the Sun," presented at SOHO14/GONG Workshop, Helio- and Astero-seismology: Towards a Golden Future, New Haven, Connecticut, USA 2004.
- [13] R. Scharstein, "Helmholtz decomposition of surface electric current in electromagnetic scattering problems," in *Proc. 23rd South-eastern Symp. Syst. Theory*, 1991, pp. 424–426.
- [14] M. Lorenzi, N. Ayache, and X. Pennec, "Regional flux analysis of longitudinal atrophy in Alzheimer's disease," in *Proc. Int. Conf. Med. Image Comput. Assisted Intervention*, 2012, pp. 739–746.

- [15] C. Luo, I. Safa, and Y. Wang, "Feature-aware streamline generation of planar vector fields via topological methods," *Comput. Graph.*, vol. 36, pp. 754–766, 2012.
- [16] B. Palit, A. Basu, and M. Mandal, "Applications of the discrete Hodge-Helmholtz decomposition to image and video processing," in *Proc. 1st Int. Conf. Pattern Recog. Machine Intell.*, 2005, pp. 497–502.
- [17] T. F. Frik and A. Roshko, "Vortical structure in the wake of a transverse jet," *J. Fluid Mech.*, vol. 279, pp. 1–47, 1994.
- [18] R. W. Grout, A. Gruber, H. Kolla, P. -T. Bremer, J. C. Bennett, A. Gyulassy, and J. H. Chen, "A direct numerical simulation study of turbulence and flame structure in transverse jets analysed in jet-trajectory based coordinates," *J. Fluid Mech.*, vol. 706, pp. 351–383, 2012.
- [19] A. Söderström, M. Karlsson, and K. Museth, "A PML-based non-reflective boundary for free surface fluid animation," *ACM Trans. Graph.*, vol. 29, no. 5, article 136, 2010.
- [20] F. Lekien, C. Coulliette, R. Bank, and J. Marsden, "Open-boundary modal analysis: Interpolation, extrapolation, and filtering," *J. Geophysical Res.*, vol. 109, 2004.
- [21] A. Wiebel, Feature detection in vector fields using the Helmholtz-Hodge decomposition, Diplomarbeit, Univ. of Kaiserslautern, Kaiserslautern, Deutschland, 2004.
- [22] W. E and J. G. Liu, "Projection Method I: Convergence and Numerical Boundary Layers," *SIAM J. Numerical Anal.*, vol. 32, no. 4, pp. 1017–1057, 1995.
- [23] F. M. Denaro, "On the application of the Helmholtz-Hodge decomposition in projection methods for incompressible flows with general boundary conditions," *Int. J. Numerical Methods Fluids*, vol. 43, pp. 43–69, 2003.
- [24] K. Polthier and E. Preuß, "Variational approach to vector field decomposition," in *Proc. Eurographics Workshop Sci. Vis.*, 2000, pp. 147–155.
- [25] K. Polthier and E. Preuß, "Identifying vector fields singularities using a discrete Hodge decomposition," in *Visualization and Mathematics III*, H.C. Hege and K. Polthier, eds., New York, NY, USA: Springer, 2003, pp. 112–134.
- [26] Y. Tong, S. Lombeyda, A. Hirani, and M. Desbrun, "Discrete multiscale vector field decomposition," *ACM Trans. Graph.*, vol. 22, no. 3, pp. 445–452, 2003.
- [27] Q. Guo, M. K. Mandal, and M. Y. Li, "Efficient Hodge-Helmholtz decomposition of motion fields," *Pattern Recog. Lett.*, vol. 26, no. 4, pp. 493–501, 2005.
- [28] F. Petronetto, A. Paiva, M. Lage, G. Tavares, H. Lopes, and T. Lewiner, "Meshless Helmholtz-Hodge decomposition," *IEEE Trans. Vis. Comput. Graph.*, vol. 16, no. 2, pp. 338–342, Mar./Apr. 2010.
- [29] J. B. Bell and D. L. Marcus, "A second-order projection method for variable-density flows," *J. Comput. Phys.*, vol. 101, pp. 334–348, 1992.
- [30] R. Fedkiw, J. Stam, and H. W. Jensen, "Visual simulation of smoke," in *Proc. 28th Annu. Conf. Comput. Graph. Interactive Techn.*, 2001, pp. 15–22.
- [31] N. Foster and D. Metaxas, "Modeling the motion of a hot, turbulent gas," in *Proc. 24th Annu. Conf. Comput. Graph. Interactive Techn.*, 1997, pp. 181–188.
- [32] A. B. Stephens, J. B. Bell, J. M. Solomon, and L. B. Hackerman, "A finite difference galerkin formulation for the incompressible Navier-Stokes equations," *J. Comput. Phys.*, vol. 53, pp. 152–172, 1984.
- [33] J. Stam, "Stable fluids," in *Proc. 26th Annu. Conf. Comput. Graph. Interactive Techn.*, 1999, pp. 121–128.
- [34] E. Deriaz and V. Perrier, "Orthogonal Helmholtz decomposition in arbitrary dimension using divergence-free and curl-free wavelets," *Appl. Comput. Harmonic Anal.*, vol. 26, no. 2, pp. 249–269, 2009.
- [35] I. Macêdo and R. Castro, "Learning divergence-free and curl-free vector fields with matrix-valued kernels," Instituto de Matemática Pura e Aplicada, Rio de Janeiro, RJ, Tech. Rep., 2010.
- [36] H. Bhatia, G. Norgard, V. Pascucci, and P.-T. Bremer, "The Helmholtz-Hodge decomposition—A survey," *IEEE Trans. Vis. Comput. Graph.*, vol. 19, no. 8, pp. 1386–1404, Jun. 2013.
- [37] A. Wiebel, C. Garth, and G. Scheuermann, "Computation of localized flow for steady and unsteady vector fields and its applications," *IEEE Trans. Vis. Comput. Graph.*, vol. 13, no. 4, pp. 641–651, Jul./Aug. 2007.
- [38] G. Arfken, *Mathematical Methods for Physicists*, 3rd ed. New York, NY, USA: Academic, 1985.
- [39] H. Margenau and G.M. Murphy, *The Mathematics of Physics and Chemistry*. New York, NY, USA: Van Nostrand, 1943.
- [40] A. J. Chorin and J. E. Marsden, *A Mathematical Introduction to Fluid Mechanics*. New York, NY, USA: Springer, 1993.
- [41] V. Girault, "Incompressible finite element methods for Navier-Stokes equations with nonstandard boundary conditions in R^3 ," *Math. Computations*, vol. 51, no. 183, pp. 55–74, 1998.
- [42] B. Cabral and L. C. Leedom, "Imaging vector fields using line integral convolution," in *Proc. 20th Annu. Conf. Comput. Graph. Interactive Techn.*, 1993, pp. 263–270.
- [43] C. S. Yoo, E. Richardson, R. Sankaran, and J. H. Chen, "A DNS study on the stabilization mechanism of a turbulent lifted ethylene jet flame in highly-heated coflow," in *Proc. of the Combustion Institute*, vol. 33, no. 1, pp. 1619–1627, 2011.
- [44] Nektar++. [Online]. Available: <http://www.nektar.info>, 2014.



Harsh Bhatia is a PhD candidate at the Scientific Computing and Imaging (SCI) Institute, University of Utah, and a research scholar at the Lawrence Livermore National Laboratory (LLNL). His research interests include topological analysis of scalar and vector fields, uncertainty visualization, graphics and visualization, and modeling and simulation. Prior to grad school, he received the BTech degree in information and communication technology from DA-ICT, India in 2007. He is a student member of IEEE.



Valerio Pascucci received the EE laurea (master's) degree from the University La Sapienza, Rome, Italy, in December 1993, as a member of the Geometric Computing Group, and the PhD degree in computer science from Purdue University, in May 2000. He is a faculty member at the Scientific Computing and Imaging (SCI) Institute, University of Utah. Before joining SCI, he served as a project leader at the Lawrence Livermore National Laboratory (LLNL), Center for Applied Scientific Computing (from May 2000) and as an adjunct professor at the Computer Science Department of the University of California, Davis (from July 2005). Prior to his tenure at CASC, he was a senior research associate at the University of Texas at Austin, Center for Computational Visualization, CS, and TICAM Departments. He is a member of the IEEE.



Peer-Timo Bremer received the PhD degree in computer science from the University of California, Davis, in 2004 and the diploma in mathematics and computer science from the Leibniz University in Hannover, Germany, in 2000. He is a computer scientist and project leader at the Center for Applied Scientific Computing, Lawrence Livermore National Laboratory (LLNL) and the associated director for Research at the Center for Extreme Data Management, Analysis, and Visualization, University of Utah. Prior to his tenure at CASC, he was a postdoctoral research associate at the University of Illinois, Urbana-Champaign. He is a member of the IEEE Computer Society and the IEEE.

► For more information on this or any other computing topic, please visit our Digital Library at www.computer.org/publications/dlib.